Structure of a bacterial cell surface decaheme electron conduit

Thomas A. Clarke[a,1], Marcus J. Edwards[a], Andrew J. Gates[a], Andrea Hall[a], Gaye F. White[a], Justin Bradley[a], Catherine L. Reardon[b], Liang Shi[b], Alexander S. Beliaev[b], Matthew J. Marshall[b], Zheming Wang[b], Nicholas J. Watmough[a], James K. Fredrickson[b], John M. Zachara[b], Julea N. Butt[a], and David J. Richardson[a,1]

[a]Centre for Molecular and Structural Biochemistry, School of Biological Sciences and School of Chemistry, University of East Anglia, Norwich NR4 7TJ, United Kingdom; and [b]Pacific Northwest National Laboratory, Richland, WA 99352

Edited by Dianne Newman, Caltech/Howard Hughes Medical Institute, Pasadena, CA, and accepted by the Editorial Board April 21, 2011 (received for review November 22, 2010)

Some bacterial species are able to utilize extracellular mineral forms of iron and manganese as respiratory electron acceptors. In *Shewanella oneidensis* this involves decaheme cytochromes that are located on the bacterial cell surface at the termini of trans-outer-membrane electron transfer conduits. The cell surface cytochromes can potentially play multiple roles in mediating electron transfer directly to insoluble electron sinks, catalyzing electron exchange with flavin electron shuttles or participating in extracellular intercytochrome electron exchange along "nanowire" appendages. We present a 3.2-Å crystal structure of one of these decaheme cytochromes, MtrF, that allows the spatial organization of the 10 hemes to be visualized for the first time. The hemes are organized across four domains in a unique crossed conformation, in which a staggered 65-Å octaheme chain transects the length of the protein and is bisected by a planar 45-Å tetraheme chain that connects two extended Greek key split β-barrel domains. The structure provides molecular insight into how reduction of insoluble substrate (e.g., minerals), soluble substrates (e.g., flavins), and cytochrome redox partners might be possible in tandem at different termini of a trifurcated electron transport chain on the cell surface.

c-type cytochromes | iron respiration | MtrC | multiheme

Many Gram-negative bacteria can couple anaerobic growth to the respiratory reduction of insoluble Fe(III) and Mn (IV) oxides (1). To exploit these abundant electron sinks, specific respiratory electron transfer mechanisms must overcome the physical limitations associated with electron transfer across the outer membrane (OM) to solid extracellular terminal electron acceptors. In *Shewanella oneidensis* this involves proteins coded by the *mtrDEF-omcA-mtrCAB* gene cluster (1, 2). MtrA and MtrB form a trans-OM electron transport complex that comprises a β-barrel porin (MtrB) in which a decaheme cytochrome (MtrA) is embedded (3, 4). MtrC forms an extracellular decaheme terminus to this complex. The MtrCAB complex has been reconstituted into sealed membrane vesicles and shown to conduct electrons across the vesicular membrane (4). MtrF, MtrD, and MtrE are homologues of MtrC, MtrA, and MtrB, respectively. The *mtrDEF* operon is most highly expressed during growth in biofilms (5), but hybrid complexes can form between MtrCAB and MtrFDE components (2, 6). The OmcA protein is a homologue of MtrC and MtrF that may be able to receive electrons from the MtrCAB or MtrFDE complexes via interaction with the decaheme termini, MtrC or MtrF (7), but can also substitute for these proteins in *mtrC mtrF* deletion mutants (2). The passage of electrons across the OM through the MtrABC or MtrDEF conduits can be viewed as electron transfer *to* the microbe-mineral interface (4). A number of possible mechanisms for electron transfer *at* the microbe-mineral interface (i.e., electron transfer from the MtrC, MtrF, or OmcA termini to an insoluble mineral substrate) have been suggested that that could occur in tandem and include (*i*) direct transfer of electrons to insoluble mineral substrates; (*ii*) indirect electron transfer mediated by flavin electron shuttles, or (*iii*) intercytochrome electron transfer, possibly along "nanowires" (8–16). Here we present the X-ray crystal structure of a decaheme terminus of an OM conduit, MtrF, and propose models from this structure into how these different types of extracellular electron transfer might occur.

Results

The X-Ray Crystal Structure of MtrF. The crystal structure of MtrF was solved to 3.2-Å resolution. At this resolution it was possible to confidently place the heme cofactors, main chain polypeptide, and majority of the side chains. The overall structure of the MtrF resembles an oblate ellipsoid with approximate dimensions of $85 \times 70 \times 30$ Å, similar to those predicted by small angle X-ray scattering for OmcA (13) (Fig. 1). MtrF is folded into four distinct domains that are formed sequentially through the amino acid (aa) sequence (Fig. 1*B* and Fig. S1). Domains I (aa 49–186) and III (aa 319–473) each contain seven antiparallel β-strands folded together through an extended Greek key topology that results in a split-barrel structure (Fig. 1*B* and Fig. S1). Domains II (aa 187–318) and IV (aa 474–641) each bind five tightly packed hemes covalently attached to the Cys residues of the five CXXCH motifs in each domain. The four domains fold together so that the pentaheme domains II and IV are packed to form a central core with the two split-barrel domains I and III flanking either side (Fig. 1*B*). Domains I and II could be superposed over domains III and IV with a rmsd difference of 2.8 Å, suggesting that the 4 domain MtrF may have arisen from a gene-duplication event of a 2-domain pentaheme protomer. In support of this view alignment of the primary structures of the domains II and IV shows similar spatial arrangement of the five CXXCH heme binding motifs (Fig. S2). There is an open cylindrical cleft with a diameter of 20 Å between domain I and IV, but a similar cleft between domains II and III is occluded by an α-helical interdomain bridge (Fig. 1*B*). Domain III also contains two cysteine residues in a CX_8C surface loop that forms a disulfide bond that is partially exposed to the solvent (Fig. 1 and Fig. S3*E*). The disulfide is 22 Å from the nearest hemes (hemes 4 and 7) and so is electronically isolated from the heme redox centers. The α-helical bridge and disulfide bond serve to maintain the overall rigidity of

Author contributions: T.A.C., J.K.F., J.M.Z., J.N.B., and D.J.R. designed research; T.A.C., M.J.E., A.J.G., A.H., G.W., J.B., C.L.R., L.S., A.S.B., M.J.M., and Z.W. performed research; N.J.W. contributed new reagents/analytic tools; T.A.C., M.J.E., A.J.G., G.F.W., J.N.B., and D.J.R. analyzed data; and T.A.C. and D.J.R. wrote the paper.

The authors declare no conflict of interest.

This article is a PNAS Direct Submission. D.N. is a guest editor invited by the Editorial Board.

Data deposition: The refined coordinates have been deposited in the Protein Data Bank, www.pdb.org (PDB ID code 3PMQ).

[1]To whom correspondence may be addressed. E-mail: tom.clarke@uea.ac.uk or D.richardson@uea.ac.uk.

This article contains supporting information online at www.pnas.org/lookup/suppl/doi:10.1073/pnas.1017200108/-/DCSupplemental.

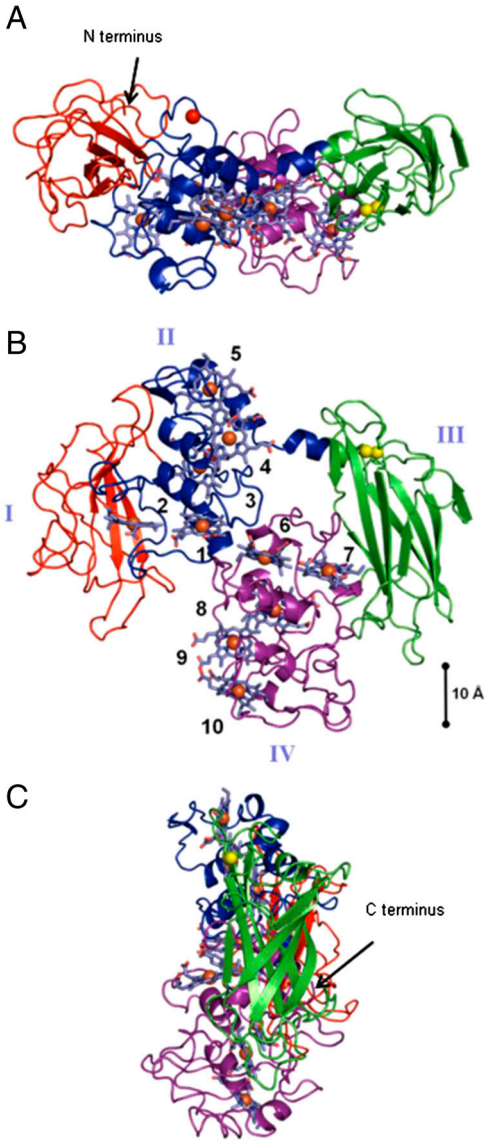

Fig. 1. Crystal structure of MtrF with the four domains colored sequentially red, blue, green, and purple from the N terminus to the C terminus. The 10 heme cofactors are colored blue. (*A*) A view of MtrF showing the positioning of all 10 hemes on one side of the molecule and the two split β-barrel domains. (*B*) A view of MtrF rotated 90° on the longitudinal axis compared to *A*. It shows the arrangement of hemes within the protein that are numbered according to their position in the peptide sequence. The disulfide bond between Cys 428 and Cys 437 is shown with sulfurs colored as yellow spheres. (*C*) A view of MtrF rotated 90° on the vertical axis compared to *B*.

domains II and III, which have average temperature factors of 87.1 and 74.9 $Å^2$, respectively, whereas the average temperature factors for domains I and IV are higher at 160 and 121 $Å^2$, respectively. The higher temperature factors cause the electron density in these regions to be less well defined due to a greater mobility of the residues in these areas. The residues modeled in domains I and IV therefore appear more disordered than in domains II and III, but are supported by the overall *R* factor and *R*-free values that are appropriate for a model at this resolution.

The 10 hemes of MtrF are organized into a unique "staggered cross," in which a staggered 65-Å octaheme chain (hemes 10, 9, 8, 6, 1, 3, 4, 5) transects the length of the protein through domains IV and II and is crossed at the middle by a 45-Å tetraheme chain (hemes 2, 1, 6, 7) that connects the two Greek key split β-barrel domains I and III (Fig. 1*B* and 2*A*). This staggered cross is made up of a lower order organization of two triads of parallel hemes (hemes 3, 4, 5 and hemes 8, 9, 10) that lie perpendicular to a quartet of parallel hemes (hemes 2, 1, 6, 7) (Fig. 2*A* and Fig. S2). Each heme is within 7 Å of its nearest neighbor(s) (Fig. 2*A*), which serves to ensure rapid electron transfer between all 10 hemes. In principle electron transfer is also possible between the hemes 2–3 and 7–8 pairs as they are positioned 11 Å apart (Fig. 2*A*). The overall surface exposure of each heme was calculated using AREAIMOL in the CCP4 package (17). In domain I, hemes 1, 2, 3, 4, and 5 have exposed surface areas of 146, 201, 18, 229, and 254 $Å^2$, respectively, whereas in domain IV hemes 6, 7, 8, 9, and 10 have exposed surface areas of 109, 226, 28, 230, and 297 $Å^2$, respectively. The average solvent exposure per heme is 173 ± 90 $Å^2$, which is similar to the average solvent exposure in small electron transfer proteins such as NrfB (181 ± 69 $Å^2$) or small tetraheme cytochrome (STC) (228 ± 59 $Å^2$) rather than the larger catalytic multiheme cytochromes such as NrfA (46 ± 28 $Å^2$) or hydroxylamine oxidoreductase (76 ± 74 $Å^2$) (18–22). Interestingly, MtrF, NrfB, and STC all have terminal hemes with solvent exposures of ~300 $Å^2$. In STC, this is heme one in the polypeptide chain (18), whereas in MtrF and NrfB, it is the last heme incorporated and has been shown in NrfB to be at the interface of the NrfA:NrfB complex (19). The overall high level of solvent exposure of the heme chains of MtrF results in a negatively charged electrostatic surface that is contributed to by the 20 heme propionates associated with the 10 bound hemes (Fig. 2 *C* and *D*). Extensive dialysis of MtrF followed by inductively coupled plasma emission analysis revealed that 18 ± 2 mol Ca^{2+} ions were bound per mol MtrF, which could serve to charge compensate this negatively charged surface. One of these Ca^{2+} ions could be identified in the crystal structure and was located close to heme 3 coordinated in a manner that suggests a structural role in orientating the residues around the heme 3 distal ligand

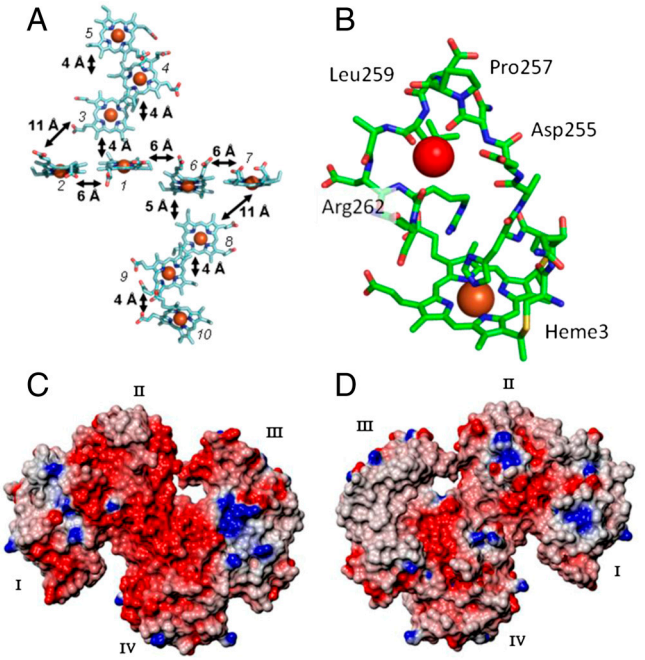

Fig. 2. Heme packing motifs within the MtrF molecule. (*A*) Arrangement of hemes within the MtrF molecule. The orientation corresponds to Fig. 1*B*, and the distances between the porphyrin rings are indicated. (*B*) Calcium binding site on the surface of MtrF with the heme and peptide displayed as sticks, the heme iron and calcium displayed as spheres. The calcium is coordinated by the carbonyl backbones of Pro 257, Leu 259, and Arg262, as well as the carboxy side chain of Asp255. (*C* and *D*) Electrostatic surface of MtrF calculated and displayed using CCP4mg. The surface potentials displayed scale from −0.5 V (red, negatively charged) to +0.5 V (blue, positively charged). (*C*) Surface of MtrF showing the charge associated with the heme propionate groups. (*D*) Opposite surface of MtrF to that shown in *C*.

that would lead to this Ca^{2+} ion being more ordered that the other Ca^{2+} ions associated with the protein (Fig. 2*B*).

The structure of MtrF raises questions about how it might interact on the membrane surface with the integral membrane MtrDE cytochrome-porin electron delivery module. Thus, the MtrF coordinates were submitted to the Protein–Protein Interface Prediction (PPI-PRED) server (23) and the Solvent accessibility-based Protein–Protein Interface iDEntification and Recognition (SPPIDER) server (24) (Fig. S3 *A* and *B*). Both analyses suggested that Domains I and IV are the most likely to be involved in making protein–protein contacts. The residues identified as potentially being involved in protein–protein contacts lie within regions with relatively high temperature factors that may result from destabilization of the structure due to the absence of the protein partner (Fig. S3*C*). To further explore sequence conservation that may be important in protein–protein interactions, 18 unique sequences (30–98% identity to target sequence) of both MtrF and MtrC homologues from *Shewanella* species were aligned with the MtrF primary structure sequence using ClustalW and the sequence conservation mapped onto the MtrF coordinates using the ConSurf server (25). A path of conserved residues followed the branched chains of hemes that include the 10 CXXCH motifs involved in heme binding and coordination. The residues involved in the domain III disulfide were also conserved. In addition, clusters of conserved residues were also observed on domains I and IV (Fig. S3*D*), suggesting a functional importance, potentially in the interactions of MtrF and MtrC with the MtrDE and MtrAB cytochrome-porin partner complexes, respectively. Thus the combined PPI-PRED, SPPIDER, and ConSurf analyses, together with the consideration of the temperature factors, suggests a model in which MtrF is configured to interact with MtrDE via domains I and IV and receive electrons into the highly solvent-exposed heme 10 at the opening of the interdomain cleft. This would then make Heme 5 a solvent-exposed electron egress site at the opposite end of the staggered octaheme chain (Fig. 3).

Relating the Spectropotentiometric Properties of MtrF to the Protein Structure. All 10 heme irons in the MtrF crystal structure display bis-His axial ligand coordination (Fig. S2 *B* and *C*). The His residue of each CXXCH motif provides the proximal ligand to the iron of the heme bound to that motif and five additional His residues in each domain provide the distal ligands for the five hemes within the same domain. Bis-His axial ligation was also supported by the solution-state near infrared magnetic circular dichroism (NIR-MCD) spectrum. This revealed a peak at 1,500 nm for oxidized MtrF that is characteristic for low-spin ferric hemes in which the Fe(III) is coordinated by two axial nitrogen atoms (e.g., from His or Lys) (Fig. 4*A*) (26). There is no evidence for a peak at 1,800 nm that would be indicative of His-Met coordination. A single low-spin bis-His coordinated heme displays NIR-MCD $\Delta\varepsilon_{1,500\,\mathrm{nm}}$ of 0.8–1.0 $\mathrm{mM^{-1}\,cm^{-1}\,T^{-1}}$ and so the intensity of the MtrF NIR-MCD spectrum (approximately 8 $\mathrm{mM^{-1}\,cm^{-1}\,T^{-1}}$) can account for all 10 hemes. The strong ligand field created by bis-His coordination generally leads to Fe(III) displaying low-spin electronic character. This is reflected in the visible spectrum of oxidized MtrF that has absorption bands at 410 nm and 530–560 nm indicative of low-spin ferric hemes (Fig. S4). The electron paramagnetic resonance (EPR) spectrum of the oxidized protein is also characteristic of low spin ($S = \frac{1}{2}$) ferric hemes because intense features at $g = 6$ expected for high spin heme are absent (Fig. 5*A*). The hemes titrated from ferric to the EPR silent ferrous forms ($S = 0$) across a window of 400 mV (Fig. 5). Spectra arising from ferric heme containing protein could be modeled with three groups of signal giving species denoted low-spin 1 (LS1), low-spin 1 (LS2), and large $g_{\max}$ (LGM) (Fig. 5*B* and Fig. S5). The intense LS1 signal is a rhombic signal with $g_{1,2,3} = 2.98$, 2.26, and 1.5 characteristic of low-spin ferric hemes with near-parallel His ligand pairs. For the fully oxidized protein spin quantitation suggested that LS1 accounted for five to six hemes, which is consistent with six MtrF hemes (hemes 2, 4, 5, 6, 7, and 8) displaying near-parallel His ligands in the crystal structure (Fig. S2). The broad potential window across which these hemes titrate, 0 to −260 mV, is also consistent with the origin of LS1 in multiple hemes, Fig. 5*C*. The broad $g = 3.26$ signal on the low field side of LS1 is typical of the broad LGM signals characteristic of low-spin hemes with near-perpendicular bis-His ligand pairs such as displayed by hemes 1, 3, or 9 in the crystal structure (Fig. S2). Quantitation of LGM for the fully oxidized protein suggests that this accounts for approximately two of these three hemes and the signal titrated between −100 and −260 mV (Fig. 5*C*), a broad window that was consistent with more than one heme contributing. The LS2 signal is a second rhombic signal, with $g_{1,2,3} = 2.83$, 2.31, and 1.63, that has greatly decreased rhombicity ($g_1 - g_3 = 1.2$) compared to LS1 ($g_1 - g_3 = 1.48$) (Fig. 5*B*). Such lower rhombicity has been observed when a ferric heme imidazole ligand deprotonates to an imidazolate (26, 27). LS2 accounts for one heme in the spectrum of fully oxidized protein. It is the only signal remaining at −260 mV and so arises from the lowest potential heme in the protein (Fig. S5). Increased solvent exposure contributes to a heme titrating at lower potentials, and so on this basis heme 10 is a strong candidate as the origin of LS2, consistent with the suggestion from the topology modeling that this heme is the

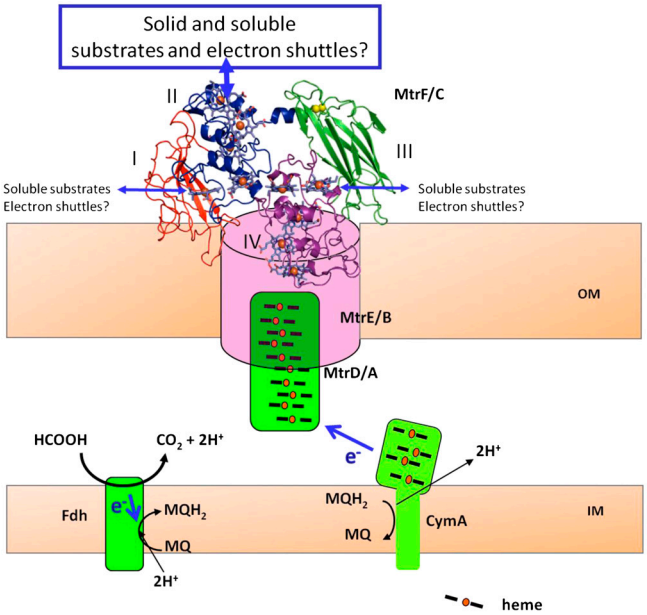

Fig. 3. Cartoon showing the possible integration of MtrF into the respiratory electron transport system. The MtrF is oriented so that domains I and IV interact with the outer-membrane MtrDE cytochrome-porin electron delivery module. This orientation positions heme 10 in domain IV to accept electrons from MtrD and heme 5 in domain II to be the solvent-exposed terminus for electron output to solid substrates, soluble substrates, or electron shuttles as suggested in the main text. The more buried hemes 2 and 7 in the domain I/II and III/IV interfaces are possible sites for electron exchange with soluble substrate or electron shuttles that could be particularly important if the heme 5 terminus is occluded by interaction with a solid surface. Electron delivery to MtrD from the inner membrane (IM) quinol pool is via the tetraheme CymA, which may be direct or via other periplasmic cytochromes that are omitted for clarity. In this illustrative cartoon electron input is shown via the formate dehydrogenase (Fdh). A transmembrane electrochemical gradient is generated across the inner membrane, whereas the extracellular respiratory substrates serve as electron sinks to recycle the menaquinone (MQ) pool. The extent to which MtrF and MtrD extend into the MtrE barrel is not known but the terminal hemes of the two proteins must come within 14 Å to allow for efficient electron transfer because the homologous MtrCAB complex has been reconstituted in proteoliposomes and shown to conduct electrons across the membrane (4).

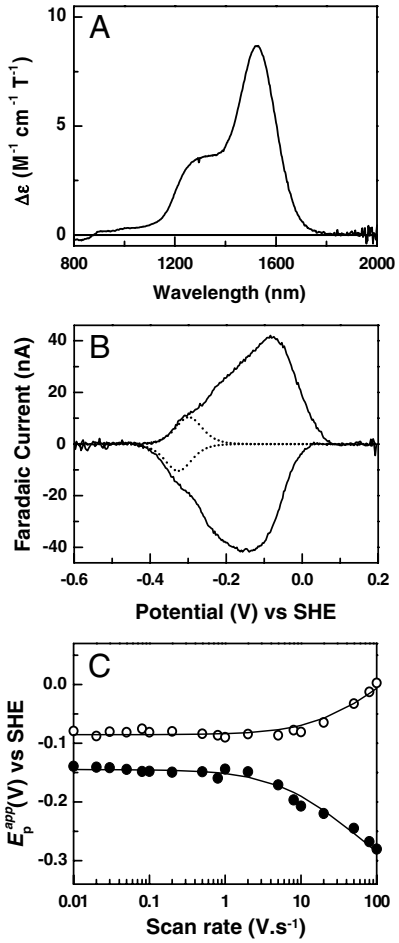

Fig. 4. Spectroscopic and voltammetric properties of MtrF. (*A*) Room temperature near infrared MCD of 95 μM MtrF in 50 mM Hepes buffer, pH* 7.0, in D_2O. The spectrum was recorded using a magnetic field of 6 T and intensity is given per protein. (*B*) PFV of MtrF: a cyclic voltammogram recorded using a freshly polished PGE electrode and immersed in 50 mM Hepes, 100 mM NaCl, pH 7.0 at 20 °C, scan rate 30 mV s^{-1}, electrode rotation 3,000 rpm. The background current was subtracted using previously described procedures (31). Fitting each peak to 10 equal $n = 1$ responses (Fig. S4) showed the low-potential flanks could be described by a single process (dotted lines) with E_m (average peak potential) of −312 mV. (*C*) Scan-rate dependence of MtrF PFV. Variation of the oxidative (open circles) and reductive (closed circles) apparent peak potentials (E_p^{app}) with scan rate. A best fit trumpet plot is shown (solid lines) with an interfacial electron exchange rate constant of 220 s^{-1}.

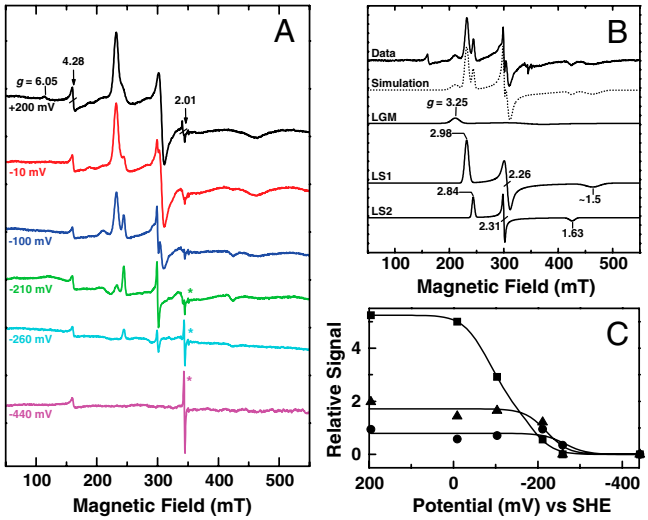

Fig. 5. (*A*) EPR monitored potentiometric titration of MtrF. CW X-band EPR (perpendicular mode) of 95 μM MtrF in 50 mM Hepes, 100 mM NaCl, 0.5% CHAPS, pH 7.5. Samples were poised in an anaerobic glove box at the potentials indicated. Spectra were recorded at 10 K, with microwave frequency, 9.68 GHz; microwave power, 2 mW; modulation amplitude, 0.1 mT (10 G). (*B*) Deconvolution of the MtrF spectrum recorded at −100 mV. Baseline subtracted (solid line) and simulated (broken line) spectra are offset for clarity. Shown below are the individual simulated line shapes for LGM, LS1, and LS2 heme populations that sum to give the simulated spectrum. (*C*) Potential dependence of the observed heme signals, LS1 (squares), LS2 (circles), and LGM (triangles). Signal area of each signal was normalized to that observed for the LS2 population. Integration of the simulated LS2 line shape from the 200-mV spectrum, relative to a 1 mM Cu^{2+}-EDTA standard, gave approximately 0.9 spins per protein. * indicates the methylviologen radical the arises from the redox mediator cocktail.

physiological electron input site. Inspection of the environment around heme 10 shows that the N_δ of the proximal His ligand is in close proximity to the Asp-361 carboxylate (~3 Å), which could lead to partial or complete deprotonation of the histidine to give it imidazolate character as seen for example on the proximal His ligand of cytochrome *c* peroxidase (28).

The ability of MtrF to rapidly exchange electrons with solid surfaces was confirmed by protein film voltammetry (PFV) (Fig. 4*B*). Cyclic voltammetry (CV) of MtrF demonstrates reversible electrochemistry over a potential window from +100 to −400 mV in agreement with the EPR monitored spectropotentiometric titration. Redox activity in this low-potential window is consistent with the bis-His coordination revealed by the crystal structure and NIR-MCD because the electron donating nature of the His ligands serves to stabilize the oxidized state of the hemes. The peaks resolved by CV were unaltered by rapid rotation of the electrode, or transfer to fresh-buffer electrolyte solution, which confirms their origin in molecules adsorbed on the surface rather than diffusing in solution. The peak areas, which reflect the number of moles of electrons exchanged between the protein and electrode, were invariant from 0.01 to 100 V s^{-1}. The separation of apparent peak potentials (E_p^{app}) increased markedly above *ca.* 5 V s^{-1}. Similar behavior has been observed for MtrC, MtrA, and OmcA (4, 29, 30). In each of these cases rigorous analysis of interfacial electron transfer kinetics is precluded by the overlapping contributions to the peaks. However, fitting the scan rate dependence of the peak potential using a Butler–Volmer description of a single, adsorbed redox center gives an indication of the rate constant for interfacial electron transfer, which for MtrF was estimated to be 220 s^{-1} (Fig. 4*C*). Inspection of the CV revealed a shoulder on the low-potential flank that was well-described by the theoretical response arising from an adsorbed center with a midpoint potential of *ca.* −312 mV exchanging one electron with the electrode and that accounts for approximately 10% of the total peak area (Fig. 4*B* and Fig. S4). Thus, the low-potential shoulder has features in good agreement with those for reduction of the lowest potential heme (the LS2 signal) identified by EPR monitored spectropotentiometry. The remaining electrochemical envelope accounted for approximately 90% of the signal (i.e., approximately nine hemes), consistent with all ten hemes of MtrF being able to communicate with the electrode either directly, or via interheme electron transfer at the scan rates studied. There is no unique fit for this region of the wave, but the data can be satisfactorily fitted to nine single-electron contributions the distribution of which are consistent with the electrochemical windows over which the hemes contributing to the LS1 and LGM signals titrated in the EPR solution-state potentiometry (Figs. S4 and S5).

The rate constants for the oxidation of reduced MtrF by FMN, a range of soluble Fe(III) complexes, and ferrihydrite were determined (Figs. S6 and S7 and Table S1). The oxidation of MtrF by solid ferrihydrite by MtrF was very slow ($k = 0.0003$ s^{-1}) and so to verify the cellular functionality of MtrF in mineral Fe(III) reduction we constitutively expressed *mtrF in trans* in a *mtrC*

omcA double mutant deficient in ferrihydrite reduction (approximately 14% of the wild-type rate) and recovered approximately 70% of the parental capacity (Fig. S6*B*). When 10 μM of FMN was added to 0.5 μM reduced MtrF (5-μM heme) the oxidation kinetics could be fitted to a single component with a second-order rate constant of 5.6×10^5 M^{-1} s^{-1} (Fig. S7). A similar value was derived on doubling the FMN concentration, suggesting that the binding site(s) is saturated at these concentrations. Inspection of the crystal structure suggests the domain I and III β-barrels are possible FMN binding sites because the extended Greek key split-barrel structure is a common in flavin binding domains (31). These two sites are structurally similar and so could be kinetically indistinguishable; however, attempts to resolve a flavin in these sites following crystal soaks or growing crystals in the presence of FMN were not successful and so the precise nature of flavin binding remains to be determined. The oxidation kinetics of reduced MtrF by Fe(III) citrate were much slower than for FMN (Fig. S7 and Table S1). For example, at 10 μM Fe (III) citrate the reaction was biphasic with second-order rate constants of 6.3×10^4 M^{-1} s^{-1} and 1×10^4 M^{-1} s^{-1}. The oxidation kinetics of reduced MtrF with $Fe(CN)_6^{3-}$ was also biphasic; the first phase had a second-order rate constant comparable to FMN, whereas the second phase was comparable to the rate of oxidation by Fe (III) citrate (Fig. S7 and Table S1). The rate of MtrF oxidation by Fe(III)EDTA and Fe(III)NTA was monophasic with second-order rate constants of 2.6×10^6 M^{-1} s^{-1} and 2.5×10^5 M^{-1} s^{-1}, respectively. It was notable that FMN oxidized only around 40% of the reduced heme groups, even at a molar ratio of 20 FMN:1 heme (Fig. S7). The $E^{0'}$ of $FMN/FMNH_2$ is approximately −200 mV (v SHE) and from the EPR and PFV analyses it was clear that only 30–40% of the hemes are oxidized at this potential, suggesting that only a subgroup of the MtrF hemes participate in FMN reduction. By contrast addition of Fe(III) citrate, Fe (III)EDTA, or Fe(III)NTA to reduced MtrF fully oxidized all 10 hemes (Fig. S7), which is consistent with an $E^{0'}$ of Fe(III)/Fe(II) of approximately +200 mV.

Discussion

We have presented the crystal structure of a member of a family of decaheme extracellular cytochromes that is widespread among Fe(III)-respiring *Shewanella* species. Although at a modest 3.2-Å resolution, the heme and domain organization evident in this structure can serve as a foundation from which to begin to explore how these extracellular termini to OM electron conduits operate at the microbe-mineral interface. With respect to electron transfer directly to insoluble electron acceptors, we have suggested a topology on the membrane surface that will need to be proven experimentally, but which suggests electron input from the cell via heme 10 and an electron egress site at the opposite end of the staggered octaheme chain at heme 5 (Fig. 3). This heme is positioned so that the edge of the porphyrin ring is exposed to the solvent (Fig. 1*B*). This configuration has been shown from modeling to be optimal for electron transfer to insoluble minerals (14) and so this heme is well placed to interact with minerals in the extracellular environment. Consistent with this, electron exchange with solid graphite electrodes probed by PFV is fast, a feature in common with OmcA and MtrC (29, 30, 32). It is then perhaps surprising that oxidation of reduced MtrF by suspensions of solid ferrihydrite is very slow. Such slow rates have also been observed for MtrC and OmcA (8) and may reflect fundamental differences in the two experiments. For example, in PFV MtrF has absorbed onto the solid electrode surface, whereas the spectrokinetic experiment is more dependent on diffusional collisions of MtrF and mineral particles. However, the differences could also reflect the importance of electron shuttles for reducing insoluble particulate materials (12).

Turning to consider electron shuttles, in the model presented, the solvent-exposed heme 5 terminus will also be able to pass electrons to high potential electron shuttles, in addition to direct reduction of a solid mineral. However, in an environment where the bacterium is interacting with a solid substrate, access to heme 5 could be sterically occluded (Fig. 3). It would then make physiological sense to have additional sites for electron egress that a soluble electron shuttle, but not a solid substrate, could access. In this context the hemes 2 and 7 termini in the Greek key split β-barrel domains I and III are intriguing. Although these could represent electron transport dead ends, it is notable that both are within 14 Å of the center of the domains that are solvent accessible. This could potentially allow electrons to be rapidly transferred to a water soluble electron acceptor that can enter these barrels (Figs. 1*A* and 2*A*). The PFV showed electrons can rapidly equilibrate across all of the MtrF hemes, and so this might enable electron exchange with a soluble substrate and an insoluble substrate to occur in tandem at hemes 2 and 7 (soluble substrates) and heme 5 (insoluble substrate) (Fig. 3). The thermodynamic domain in which FMN operates is consistent with an electron shuttle role because it needs to be sufficiently oxidizing to extract reductant from MtrF, but sufficiently reducing to enable it to pass on these electrons to an Fe(III) complex. MtrF having electron output termini tuned to the approximately −200 mV thermodynamic domain of $FMN/FMNH_2$ would make functional sense in this context. It is then possible that electron transfer from heme 10 to hemes 2 and 7 represent low-potential branches of the MtrF heme network with termini tuned for FMN reduction, whereas hemes 1, 3, 4, and 5 represent a higher potential branch suitable for electron transfer to Fe(III) minerals. The apparent saturation of the FMN binding site(s) at 10 μM is consistent with the low (approximately 0.2 μM) concentration of FMN found in cultures of *S. oneidensis* (10, 33). Fe(III) EDTA and Fe(III) NTA both rapidly oxidize MtrF at rates that can be fitted by single rate constants similar to those observed for MtrC (12). Fe(III) citrate represents an interesting soluble chelate because, although water soluble, it is bulky and would most likely experience steric hindrance for access to the more buried heme termini (12). This could reflect the much slower rate constant measured for this substrate than for FMN under identical experimental conditions.

Table 1. Collection and refinement statistics for MtrF

	SAD data	Native data
Data collection*		
Wavelength, Å	1.73	1.072
Resolution, Å	90–4.0 (4.22–4.00)	40–3.2 (3.37–3.20)
Unique reflections	23,881 (3437)	45,477 (6605)
Completeness, %	100.0 (100.0)	98.5 (98.6)
Anomalous completeness, %	100.0 (100.0)	—
R_{sym}, %	23.4 (50.5)	8.9 (41.1)
R_{pim}, %	6.9 (14.8)	5.1 (21.3)
$\langle I/\sigma \rangle$	3.1 (1.5)	6.3 (1.8)
Multiplicity	24.3 (24.6)	3.8 (3.8)
Anomalous multiplicity	12.5 (12.6)	—
Overall figure of merit	0.593	—
Refinement*,†		
R_{cryst}		30.5%
R_{free}		32.1%
Model		
Protein atoms		4,396
Haem atoms		430
Calcium atoms		1
Bond length rmsd, Å		0.005
Bond angle rmsd, °		1.12
Average *B* factor, $Å^2$		106

*Values in parentheses indicate the highest resolution shell.

†$R = |F_o - F_c|/F_o$. R_{cryst} is calculated with the 95% of data used during refinement. R_{free} is calculated with a 5% subset of data not used during refinement.

Finally we consider interprotein electron transfer with other extracellular cytochromes. Extracellular electron exchange between outer-membrane cytochromes has been demonstrated in solution for MtrC and OmcA (7). Considering the structure of MtrF, such electron transfer could be envisaged via the solvent-exposed heme 5 putative electron egress site of one monomer and a heme 10 input site of another monomer (Fig. 3). The insulating effect of the β-barrels would prevent electron exchange via the hemes 2 and 7 termini of different monomers (Fig. 3). If such interactions occurred on the cell surface, then conductive cytochrome chains could extend away from the cell, perhaps stabilized on nanowire pilli-type appendages, which in *S. oneidensis* are dependent on the MtrC and OmcA decaheme cytochromes for electrical conductance (34, 35). Further biophysical work is now required to interrogate the validity of these mechanistic models, but this first structure of a member of the extracellular decaheme cytochrome family opens up many previously undescribed experimental lines with which to move the understanding of electron transfer at the microbe-mineral interface forward.

Materials and Methods

The *mtrF* gene was amplified by PCR, cloned into pBAD202D (Invitrogen), and transformed into *S. oneidensis* MR-1. Cultures were grown aerobically in Luria–Bertani medium (30 $\mu g\,mL^{-1}$ kanamycin), and *mtrF* expression was induced by the addition of 1 mM arabinose. Purification of MtrF, kinetic, EPR, MCD, and PFV analysis were similar to those described previously for studies on MtrC and OmcA (4, 31, 36). MtrF crystals were obtained by vapor diffusion using a 1:1 mixture of 5 $mg\,mL^{-1}$ MtrF and a mother liquor of 100 mM N-(2-acetamido)iminodiacetate buffer pH 6.5, 15% ethylene glycol, 1.1 M $(NH_4)_2HPO_4$. Data were collected on frozen crystals on beamline I-02 at Diamond. A SAD (single-wavelength anomalous dispersion) dataset was collected using an x-ray wavelength of 1.73 Å at the iron K edge to a final resolution of 4.0 Å. A further dataset was collected to a resolution of 3.20 Å using an X-ray wavelength of 1.072 Å. Datasets were processed using IMOSFLM and SCALA as part of the CCP4 package (16) (Table 1). The structure of MtrF was determined through SAD phasing using SHELX to identify 10 iron sites and is described in detail in the *SI Text* (37). Electron density maps calculated using experimentally determined phases were sufficiently interpretable to manually place all 10 hemes and corresponding CXXCH motifs as well as 95% of the polypeptide backbone using COOT (38) (Fig. S8). Molecular replacement using PHASER (39) was used to fit the model to a second dataset at 3.2 Å (Fig. S3*E*). Further residues and all side chains were then built in using alternating rounds of manual building and translation liberation screw refinement with PHENIX (40). The final model was refined to R_{cryst} and R_{free} values of 30.5% and 32.1%, respectively, and has 20 residues (3.5%) in the disallowed region of the Ramachadran plot.

ACKNOWLEDGMENTS. We are grateful to Jeff McClean, Allister Crow, and Andrew Hemmings for invaluable input. This research was supported the Biotechnology and Biological Sciences Research Council (H007288/1) and the EMSL Scientific Grand Challenge project at the W. R. Wiley Environmental Molecular Sciences Laboratory, a national scientific user facility sponsored by the US Department of Energy, Office of Biological and Environmental Research program located at Pacific Northwest National Laboratory. The Pacific Northwest National Laboratory is operated for the Department of Energy by Battelle. D.J.R. is a Royal Society Wolfson Foundation Merit Award holder. T.A.C. is a Research Council U.K. Fellow.

1. Shi L, Squier TC, Zachara JM, Fredrickson JK (2007) Respiration of metal (hydr)oxides by *Shewanella* and *Geobacter*: A key role for multihaem *c*-type cytochromes. *Mol Microbiol* 65:12–20.
2. Coursolle D, Gralnick JA (2010) Modularity of the Mtr respiratory pathway of *Shewanella oneidensis* strain MR-1. *Mol Microbiol* 77:995–1008.
3. Ross DE, et al. (2007) Characterization of protein-protein interactions involved in iron reduction by *Shewanella oneidensis* MR-1. *Appl Environ Microbiol* 73:5797–7808.
4. Hartshorne RS, et al. (2009) Characterization of an electron conduit between bacteria and the extracellular environment. *Proc Natl Acad Sci USA* 106:22169–22174.
5. McLean JS, et al. (2008) Oxygen-dependent autoaggregation in *Shewanella oneidensis* MR-1. *Environ Microbiol* 10:1861–1876.
6. Bücking C, Popp F, Kerzenmacher S, Gescher J (2010) Involvement and specificity of *Shewanella oneidensis* outer membrane cytochromes in the reduction of soluble and solid-phase terminal electron acceptors. *FEMS Microbiol Lett* 306:144–151.
7. Shi L, et al. (2006) Isolation of a high-affinity functional protein complex between OmcA and MtrC: Two outer membrane decaheme *c*-type cytochromes of *Shewanella oneidensis* MR-1. *J Bacteriol* 188:4705–4714.
8. Ross DE, Brantley SL, Tien M (2009) Kinetic characterization of OmcA and MtrC, terminal reductases involved in respiratory electron transfer for dissimilatory iron reduction in *Shewanella oneidensis* MR-1. *Appl Environ Microbiol* 75:5218–5226.
9. Coursolle D, Baron DB, Bond DR, Gralnick JA (2010) The Mtr respiratory pathway is essential for reducing flavins and electrodes in *Shewanella oneidensis*. *J Bacteriol* 192:467–474.
10. Marsili E, et al. (2008) *Shewanella* secretes flavins that mediate extracellular electron transfer. *Proc Natl Acad Sci USA* 105:3968–3973.
11. Ruebush SS, Brantley SL, Tien M (2006) Reduction of soluble and insoluble iron forms by membrane fractions of Shewanella oneidensis grown under aerobic and anaerobic conditions. *Appl Environ Microbiol* 72:2925–2935.
12. Wang Z, et al. (2008) Kinetics of reduction of Fe(III) complexes by outer membrane cytochromes MtrC and OmcA of *Shewanella oneidensis* MR-1. *Appl Environ Microbiol* 74:6746–6755.
13. Johs A, Shi L, Droubay T, Ankner JF, Liang L (2010) Characterization of the decaheme *c*-type cytochrome OmcA in solution and on hematite surfaces by small angle x-ray scattering and neutron reflectometry. *Biophys J* 98:3035–3043.
14. Kerisit S, Rosso KM, Dupuis M, Valiev M (2007) Molecular computational investigation of electron-transfer kinetics across cytochrome-iron oxide interfaces. *J Phys Chem C Nanomater Interfaces* 111:11363–11375.
15. Jensen HM, et al. (2010) Engineering of a synthetic electron conduit in living cells. *Proc Natl Acad Sci USA* 107:19213–19218.
16. Lies DP, et al. (2005) *Shewanella oneidensis* MR-1 uses overlapping pathways for iron reduction at a distance and by direct contact under conditions relevant for biofilms. *Appl Environ Microbiol* 71:4414–4426.
17. Collaborative Computational Project, Number 4 (1994) The CCP4 suite: Programs for protein crystallography. *Acta Crystallogr D Biol Crystallogr*, 50 pp:760–763.
18. Leys D, et al. (2002) Crystal structures at atomic resolution reveal the novel concept of "electron-harvesting" as a role for the small tetraheme cytochrome *c*. *J Biol Chem* 277:35703–35711.
19. Clarke TA, Cole JA, Richardson DJ, Hemmings AM (2007) The crystal structure of the pentahaem *c*-type cytochrome NrfB and characterization of its solution-state interaction with the pentahaem nitrite reductase NrfA. *Biochem J* 406:19–30.
20. Bamford VA, et al. (2002) Structure and spectroscopy of the periplasmic cytochrome *c* nitrite reductase from *Escherichia coli*. *Biochemistry* 41:2921–2931.
21. Einsle O, et al. (1999) Structure of cytochrome *c* nitrite reductase. *Nature* 400:476–480.
22. Igarashi N, Moriyama H, Fujiwara T, Fukumori Y, Tanaka N (1997) The 2.8 Å structure of hydroxylamine oxidoreductase from a nitrifying chemoautotrophic bacterium, *Nitrosomonas europaea*. *Nat Struct Biol* 4:276–284.
23. Bradford JR, Westhead DR (2005) Improved prediction of protein-protein binding sites using a support vector machines approach. *Bioinformatics* 21:1487–1494.
24. Porollo A, Meller J (2007) Prediction-based fingerprints of protein-protein interactions. *Proteins* 66:630–45.
25. Ashkenazy H, Erez E, Martz E, Pupko T, Ben-Tal N (2010) ConSurf 2010: Calculating evolutionary conservation in sequence and structure of proteins and nucleic acids. *Nucleic Acids Res* 38:W529–W533.
26. Gadsby PMA, Thomson AJ (1990) A theoretical model of the intensity of near-infrared porphyrin-to-iron charge-transfer transitions in low spin iron(III) hemoproteins. A correlation between the intensity of the magnetic circular dichroism bands and the rhombmic distortion parameter of iron. *J Chem Soc Dal Trans* 1921–1928.
27. Thomson AJ, Gadsby PMA (1982) Identification of the imidazolate anion as a ligand in met-myoglobin by near-infrared magnetic circular dichroism spectroscopy. *FEBS Lett* 150:59–62.
28. Goodin DB, McRee DE (1993) The Asp-His-Fe triad of cytochrome *c* peroxidase controls the reduction potential, electronic structure, and coupling of the tryptophan free radical to the heme. *Biochemistry* 32:3313–3324.
29. Hartshorne RS, et al. (2007) Characterization of *Shewanella oneidensis* MtrC: A cell-surface decaheme cytochrome involved in respiratory electron transport to extracellular electron acceptors. *J Biol Inorg Chem* 12:1083–1094.
30. Firer-Sherwood M, Pulcu GS, Elliott SJ (2008) Electrochemical interrogations of the Mtr cytochromes from Shewanella: Opening a potential window. *J Biol Inorg Chem* 13:849–854.
31. Hubbard TJ, Ailey B, Brenner SE, Murzin AG, Chothia C (1999) SCOP: A strucutral classification of proteins database. *Nucleic Acids Res* 27:254–256.
32. Field SJ, et al. (2000) Purification and magneto-optical spectroscopic characterization of cytoplasmic membrane and outer membrane multiheme *c*-type cytochromes from *Shewanella frigidimarina* NCIMB400. *J Biol Chem* 275:8515–8522.
33. von Canstein H, Ogawa J, Shimizu S, Lloyd JR (2007) Secretion of flavins by *Shewanella species* and their role in extracellular electron transfer. *Appl Environ Microbiol* 74:615–623.
34. Gorby YA, et al. (2006) Electrically conductive bacterial nanowires produced by *Shewanella oneidensis* strain MR-1 and other microorganisms. *Proc Natl Acad Sci USA* 103:11358–11363.
35. El-Naggar MY, et al. (2010) Electrical transport along bacterial nanowires from *Shewanella oneidensis* MR-1. *Proc Natl Acad Sci USA* 107:18127–18131.
36. Shi L, Lin JT, Markillie LM, Squier TC, Hooker BS (2005) Overexpression of multi-heme *C*-type cytochromes. *Biotechniques* 38:297–299.
37. Sheldrick GM (2008) SHELXL97 and SHELXS97, programs for crystal structure solution and refinement. *Acta Crystallogr A* 64:112–122.
38. Emsley P, Cowtan K (2004) Coot: Model-building tools for molecular graphics. *Acta Crystallogr D Biol Crystallogr* 60:2126–2132.
39. McCoy AJ, et al. (2007) *Phaser* crystallographic software. *J Appl Crystallogr* 40:658–674.
40. Adams PD, et al. (2010) PHENIX: A comprehensive Python-based system for macromolecular structure solution. *Acta Crystallogr D Biol Crystallogr* 66:213–221.